

In situ study of the formation mechanism of two-dimensional superlattices from PbSe nanocrystals

4 Jaco J. Geuchies^{1,5a†}, Carlo van Overbeek^{1†}, Wiel H. Evers^{2,3}, Bart Goris⁴, Annick de Backer⁴, Anjan P.
5 Gantapara⁶, Freddy. T. Rabouw¹, Jan Hilhorst^{5b}, Joep L. Peters¹, Oleg Konovalov^{5a}, Andrei V.
6 Petukhov^{7,8}, Marjolein Dijkstra⁶, Laurens D.A. Siebbeles², Sandra van Aert⁴, Sara Bals⁴ and Daniel
7 Vanmaekelbergh^{1*}

8

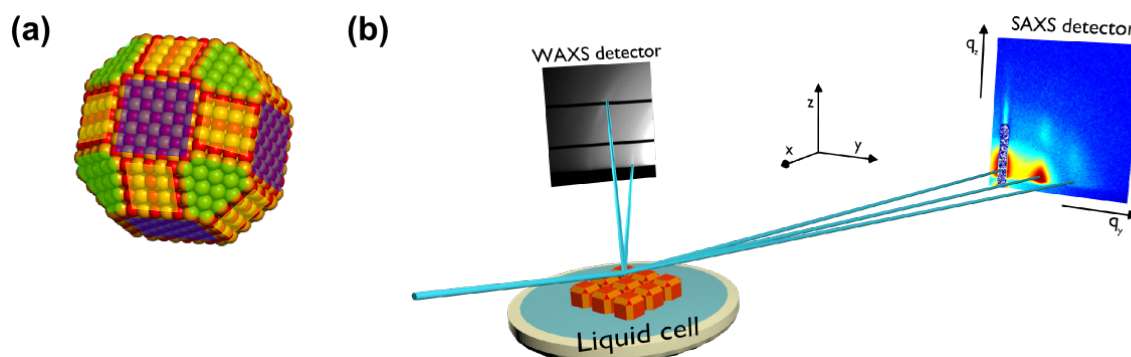
9 *Corresponding author. E-mail: d.vanmaekelbergh@uu.nl

10

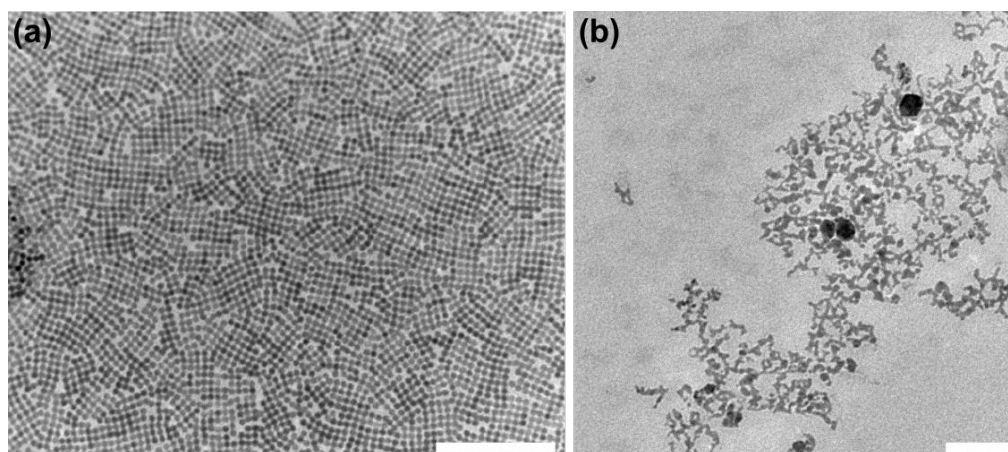
11 This supplement contains:

12	Supplementary figure S1.....	p. 3
13	Supplementary figure S2.....	p. 3
14	Supplementary figure S3.....	p. 4
15	Supplementary figure S4.....	p. 4
16	Supplementary figure S5.....	p. 5
17	Supplementary figure S6.....	p. 5
18	Supplementary figure S7.....	p. 6
19	Supplementary figure S8.....	p. 6
20	Supplementary figure S9.....	p. 7
21	Supplementary figure S10.....	p. 7
22	Supplementary figure S11.....	p. 7
23	Supplementary methods 1: calculation of the X-ray penetration depth.....	p. 9
24	Supplementary figure S12.....	p. 9
25	Supplementary methods 2: computer aided image analysis.....	p. 10
26	Supplementary figure S13.....	p. 10
27	Supplementary figure S14.....	p. 11
28	Supplementary figure S15.....	p. 11
29	Supplementary figure S16.....	p. 12
30	Supplementary methods 3: modelling of GISAXS patterns for hexagonal, rhombic and square superlattices.....	p. 13
31	Supplementary figure S17.....	p. 14
32	Supplementary methods 4: calculation of the position of the atomic reflections on the GIWAXS detector.....	p. 15
33	Supplementary figure S18.....	p. 16
34	Supplementary methods 5: peak width of atomically aligned, but not attached, nanocrystals.....	p. 17

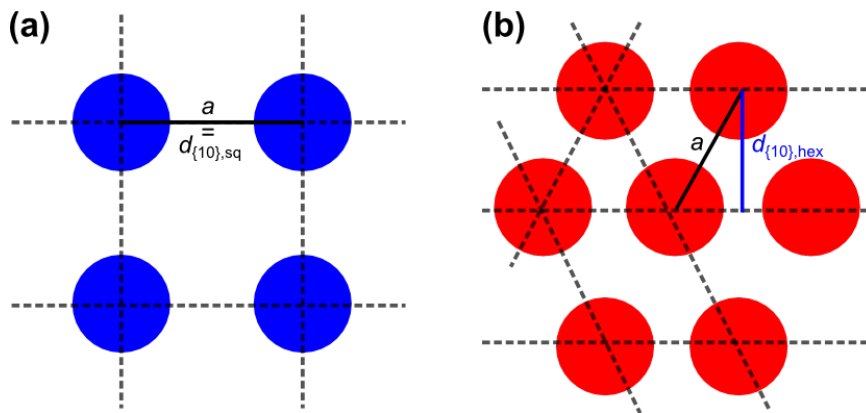
35	Supplementary figure S19.....	p. 17
36	Supplementary figure S20.....	p. 18
37	Supplementary methods 6: azimuthal and radial peak widths in electron diffraction.....	p. 20
38	Supplementary figure S21.....	p. 20
39	Supplementary figure S22.....	p. 21
40	Supplementary figure S23.....	p. 21
41	Supplementary methods 7: Coulombic and Van Der Waals interactions between nanocrystals.....	p. 22
42	Supplementary figure S24.....	p. 22
43	Supplementary figure S25.....	p. 23
44	References.....	p. 24



45 **Figure S1: Schematic of the in-situ GISAXS/GIWAXS study of nanocrystal assembly at the liquid/air**
 46 **interface. (a)** An atomic model of the PbSe truncated nanocubes, showing the different facets of the
 47 NC. Blue indicates the {100} facets, yellow the {110} facets and green the {111} facets. **(b)** Schematic
 48 of the setup used for in-situ GISAXS/WAXS experiments. A dispersion of NCs in toluene evaporates in a
 49 liquid sample cell. We examine the process of assembly and attachment using grazing-incidence x-
 50 ray scattering, by simultaneously monitoring the atomic order on the wide-angle detector and
 51 nanoscale order on the small-angle detector.

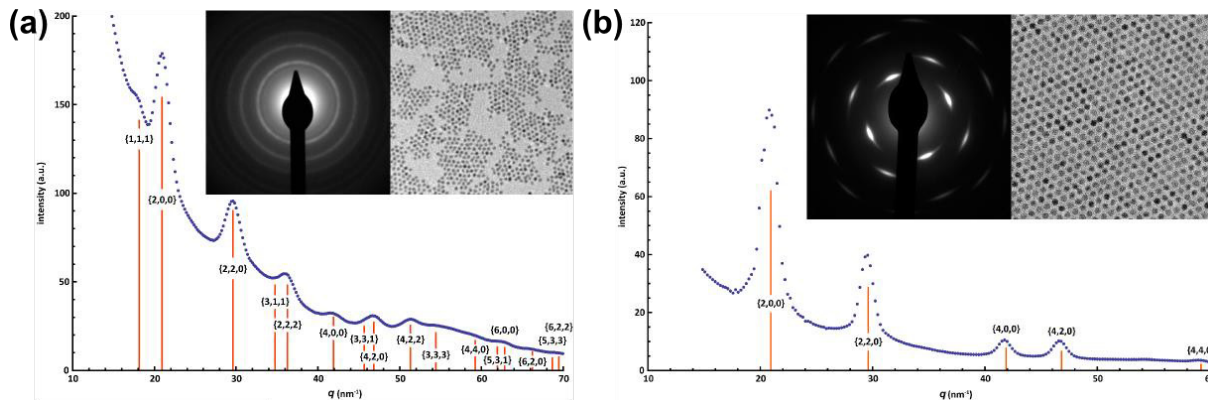


52 **Figure S2: Diffusion limited attachment of PbSe NCs results in structures with no long-range**
 53 **nanoperiodic nor atomic order. (a)** Sample where a large amount of simultaneous nucleation has
 54 taken place resulting in small domains with square geometry. **(b)** Sintered structures, with no long-
 55 range nanoperiodic or atomic order. Scale bars equal 100 nm.

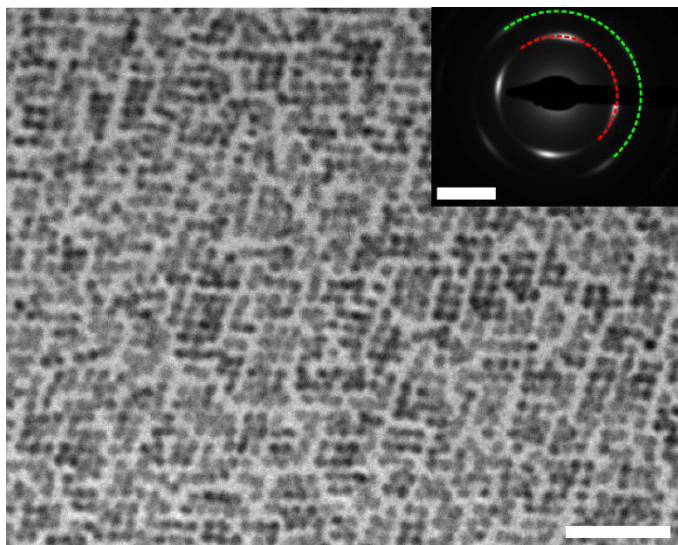


56 **Figure S3: Origin of the first diffraction rod in GISAXS and its relationship to the NC-NC distance.** (a) In
 57 the case of square ordered superlattices, the NC-NC distance a is equal to the d -spacing of the first
 58 lattice plane $d_{\{10\},sq}$. The corresponding q -vector is $q_{\{10\},sq} = 2\pi/d_{\{10\},sq} = 2\pi/a$. (b) For an
 59 hexagonal monolayer of NCs, the lattice spacing is not equal to the NC-NC distance; $d_{\{10\},hex} =$
 60 $\sqrt{3}a/2$. The corresponding q -vector then equals $q_{\{10\},hex} = 2\pi/d_{\{10\},hex} = 4\pi/(\sqrt{3}a)$. Comparing
 61 the square and hexagonal lattices, the q -vector relationship for the first diffraction is different by a
 62 term $2/\sqrt{3}$. In general the position of any GISAXS reflection in the horizontal scattering direction q_y
 63 with miller indices $\{h, k\}$ for a square lattice is equal to $q_{\{h,k\},sq} = \frac{2\pi}{a}\sqrt{h^2 + k^2}$, while for an 2-D
 64 hexagonal lattice it equals

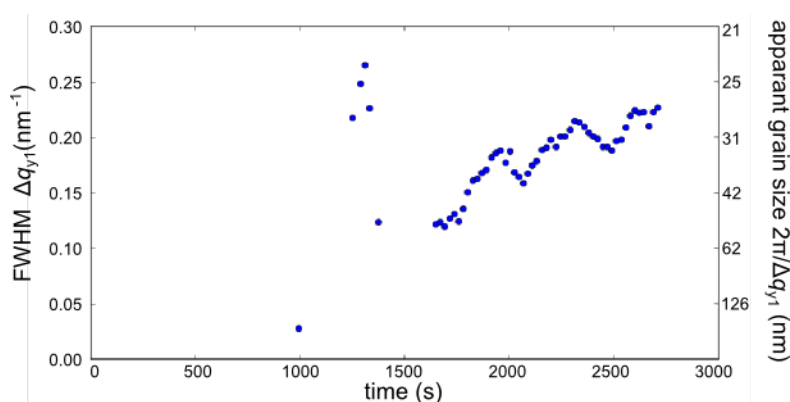
65
$$q_{\{h,k\},hex} = \frac{4\pi}{\sqrt{3}a}\sqrt{h^2 + k^2 + hk}.$$



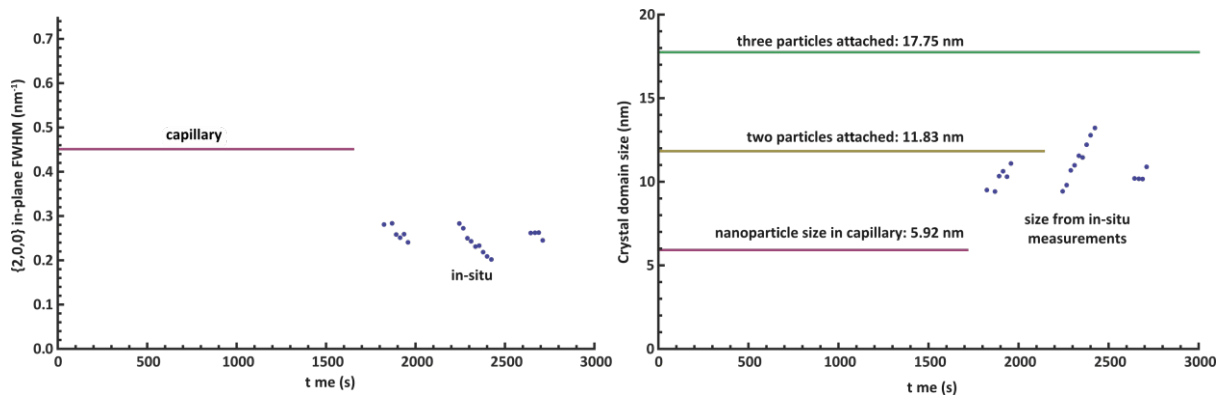
66
 67 **Figure S4: Azimuthally integrated electron diffraction patterns.** The insets are the same images as (a)
 68 Fig. 1a and (b) Fig. 1g from the main text. Orange bars denote the positions of the atomic diffraction
 69 from PbSe (PDF card #00-006-0354). (a) All atomic reflections are visible, which indicates that the
 70 particles are not aligned with respect to the electron beam. (b) Only atomic reflections for
 71 nanocrystals with their $\langle 100 \rangle$ direction perpendicular to the substrate are observed.



72 **Figure S5: Characteristic TEM image of the sample scooped from the surface used in the in-situ**
 73 **experiments shown in Fig. 2 of the main text.** Note the resemblance to Fig. 2(g). The micrograph shows
 74 that the NCs have assembled into a square superlattice. The NCs are atomically attached only in
 75 relatively small separate patches of 10-30 NCs, which could explain the peak broadening and absence
 76 of higher order diffraction rods in the GISAXS patterns. The electron diffraction pattern shows
 77 diffraction arcs, indicating atomic alignment of the particles. The coloured rings index the diffraction
 78 spots: red = {200} and green = {220}. Scalebars denote 50 nm in the TEM image and 20 nm^{-1} in the
 79 diffraction pattern. We should remark here that the formation of rather small domains that are
 80 atomically aligned has to do with the conditions under which in-situ measurements are done. Under
 81 better controlled conditions μm -large atomically coherent domains are observed (see e.g. figures S8).

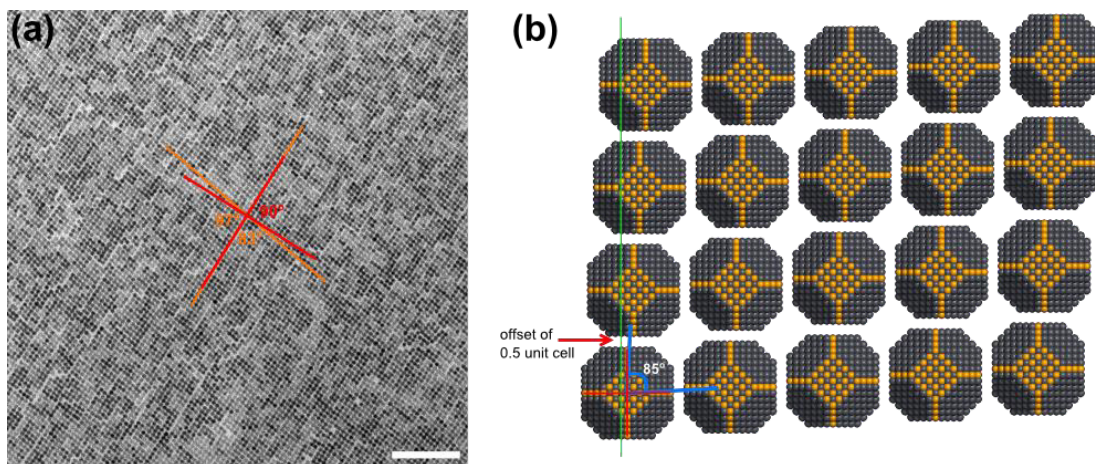


82 **Figure S6: Analysis of the peak width of the first diffraction rod in the horizontal scattering direction**
 83 **Δq_{y1} during the GISAXS experiments shown in Fig. 2 of the main text.** The grain size is calculated as
 84 $2\pi/\Delta q_{y1}$, which corresponds to the Scherrer equation with $K=1$ if you realize that $\Delta q = 4\pi/\lambda \cos(\theta)$
 85 $\Delta(2\theta)/2$. To reduce X-ray beam damage on the sample we scanned the sample perpendicular to the
 86 incoming X-ray beam over an area of 4 mm. The peak widths are likely to come from superlattice
 87 grains on the sample with slightly different sizes.

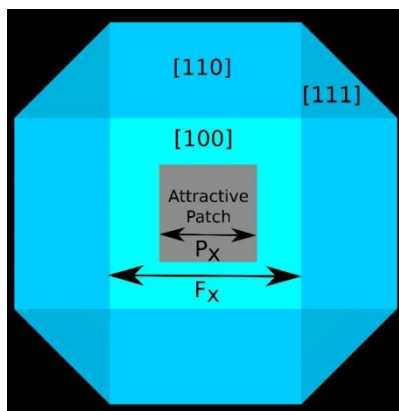


88 **Fig S7: Evolution of the peakwidth of the horizontal {200} atomic reflection over time.** Due to the large
 89 amount of experimental data, bad fits of the intensity profile were rejected from further analysis. **(a)**
 90 FWHM of the in-plane atomic {200} reflection over time. The purple line indicates the FWHM of the
 91 {200} diffraction of NCs dispersed in toluene, measured in a capillary. **(b)** The crystalline size is
 92 calculated as $2\pi/\Delta q$, which corresponds to the Scherrer equation with $K=1$ if you realize that $\Delta q =$
 93 $4\pi/\lambda \cos(\theta) \Delta(2\theta)/2$.

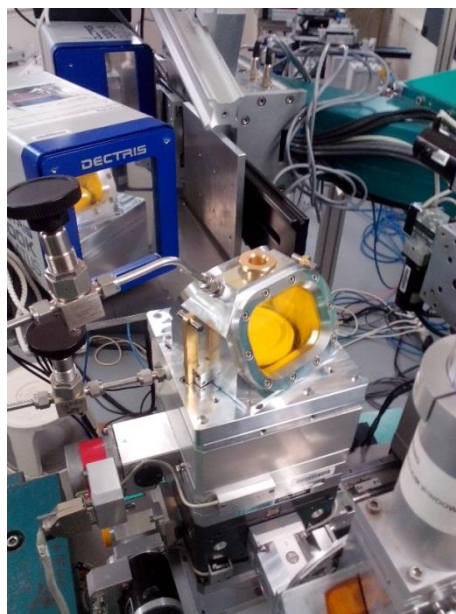
94 The crystalline size (5.92 nm) is in good agreement with the particle size obtained from TEM (5.7 ± 0.6
 95 nm). The blue dots represent the FWHM of the same atomic reflection during the in-situ experiments.



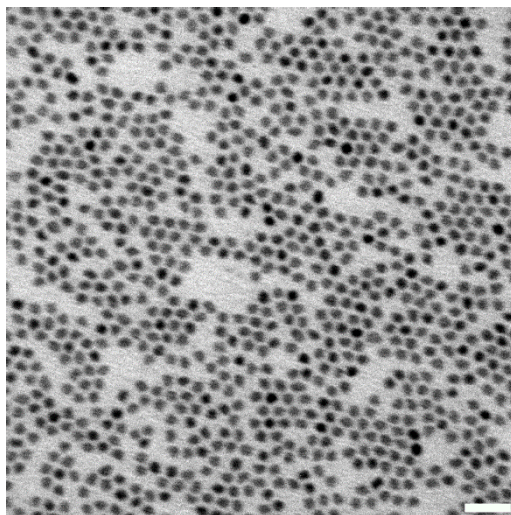
96 **Figure S8: Discussion on the bond-angles in the final square superlattices.** Due to the crystal structure
 97 of the individual PbSe nanocrystals, a shift of 0.5 unit cells in the two lateral directions is required to
 98 result in Pb-to-Se binding. The resulting bond angles would then be slightly larger or slightly smaller
 99 than 90° . **(a)** TEM image of a superlattice, where the deviation of the bond angles ($83^\circ/97^\circ$) with a
 100 perfect square lattice (90°) is clearly seen over longer distances. **(b)** Models of the PbSe nanocrystals
 101 in a square superlattice, where in both lateral directions the particles are shifted by half a unit cell.
 102 The scale bar in the TEM image equals 100 nm.



103 **Figure S9: Model of the cantellated nanocube used in our NVT simulations.** Different facets are
104 indicated along with the attractive patch on the [100] facets. Dimension of the patch P_x and the [100]
105 facet F_x are also indicated.



106 **Figure S10: Photograph of the home-built liquid cell and setup used for the in-situ GISAXS/WAXS**
107 **experiments at ID10 of the European Synchrotron Radiation Facility.** The energy of the incident X-ray
108 beam was set at 10.0 keV, below the Pb and Se absorption edges to minimize beam damage. We
109 optimized the grazing angle to 0.3° for the best signal-to-noise ratio on both GIWAXS and GIWAXS
110 detectors. As the PbSe NCs proved to be sensitive to beam damage, we scanned the sample position
111 in between the measurement, back and forth over a distance of 4 mm (in 21 steps) in the direction
112 perpendicular to the incident X-ray beam. In this way, the dose of X-ray photons on each position of
113 the sample was minimized. Each frame was recorded with a 10 s integration time, after which the
114 position of the sample was changed. After each sequence of 21 positions, we returned to the starting
115 position and repeated the procedure.



116 **Figure S11:** TEM image of the as-synthesized PbSe nanocrystals, with a diameter of 5.7 ± 0.6 nm.

117 **Supplementary methods 1: calculation of the X-ray penetration depth**

118 The incident X-ray energy of 10 keV corresponds to a wavelength $\lambda_0 = 0.124$ nm and a wavevector of
 119 magnitude $k_0 = 2\pi/\lambda_0 = 50.7$ nm⁻¹ in air. For our experiments we used a grazing angle of incidence
 120 of 0.3°, slightly larger than the critical angle for total external reflection of bulk PbSe. Since the
 121 refractive index of any material is negative at X-ray frequencies ($n = 1 - \delta + i\beta$), the wavevector
 122 inside the sample $k = nk_0$ is smaller than in air. Upon transmission of the beam into the sample, the
 123 wavevector component parallel to the air–sample interface $k_{\parallel} = k_0 \cos(\alpha_i)$ is conserved. The
 124 wavevector component perpendicular to the sample is

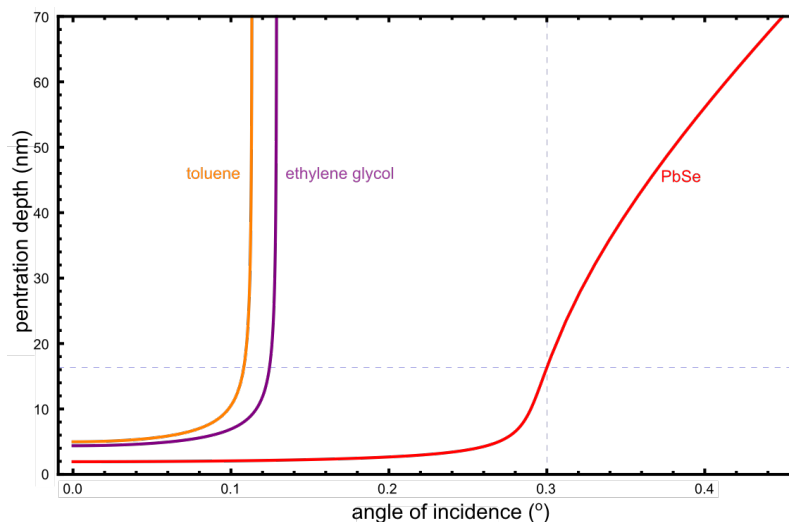
$$k_z = \sqrt{k^2 - k_{\parallel}^2} = k_0 \sqrt{n^2 - \cos^2(\alpha_i)}$$

125 Since n is complex, k_z is complex. The imaginary part of k_z describes how quickly the X-ray intensity
 126 decays when going deeper into the sample. The penetration depth d , defined as the depth at which
 127 the X-ray intensity is lower by a factor e than at the interface, is given by

$$d = \frac{1}{2 \operatorname{Im}(k_z)}$$

	δ	β
PbSe	1.292×10^{-5}	8.430×10^{-7}
Toluene	1.964×10^{-6}	1.750×10^{-9}
Ethylene glycol	2.539×10^{-6}	4.188×10^{-9}

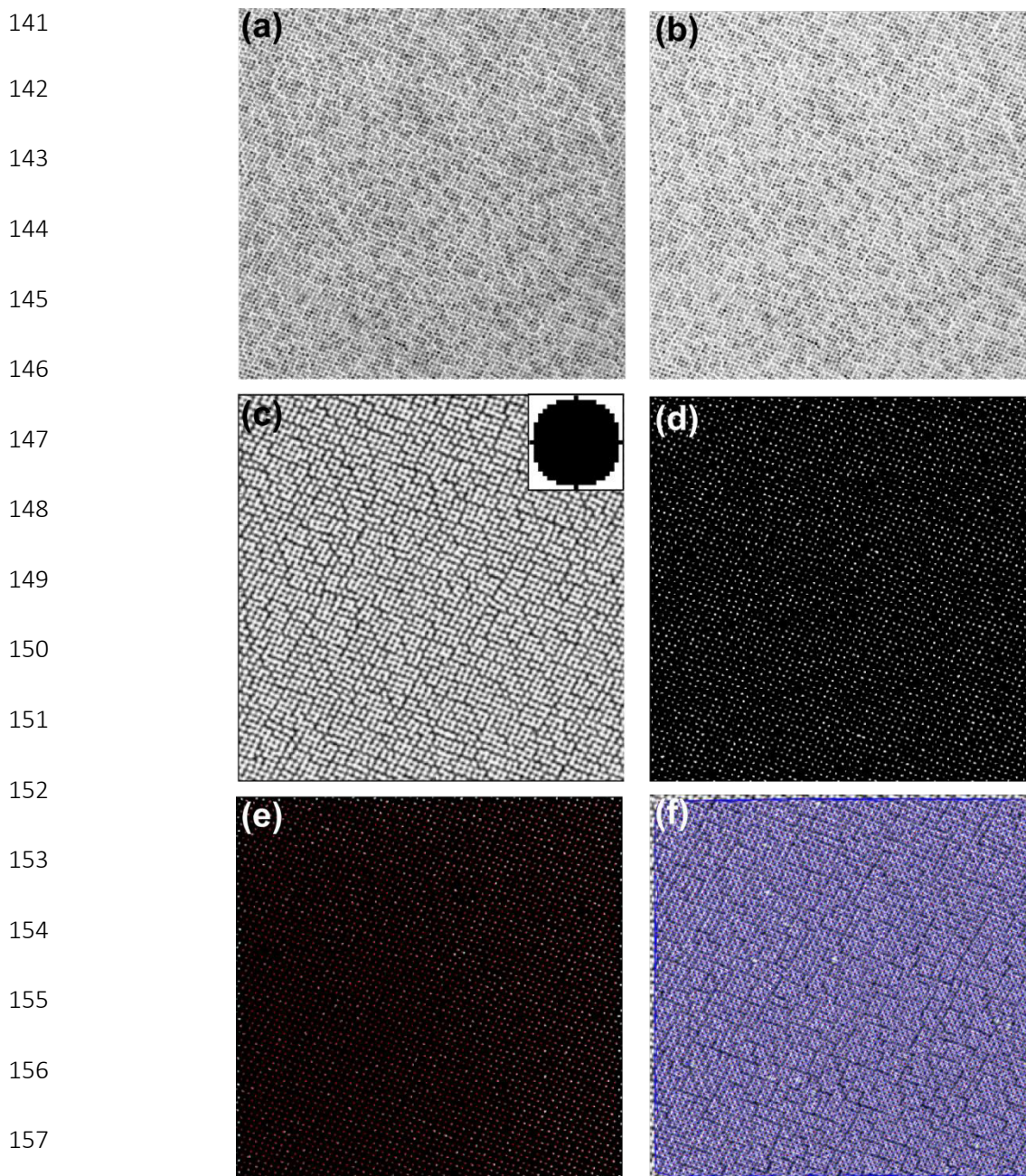
128 **Supplementary table S1:** Values of the real (δ) and imaginary (β) part of the refractive-index
 129 decrement at 10keV for the materials used in these experiments. δ and β define refraction and
 130 absorption in a material accordingly.



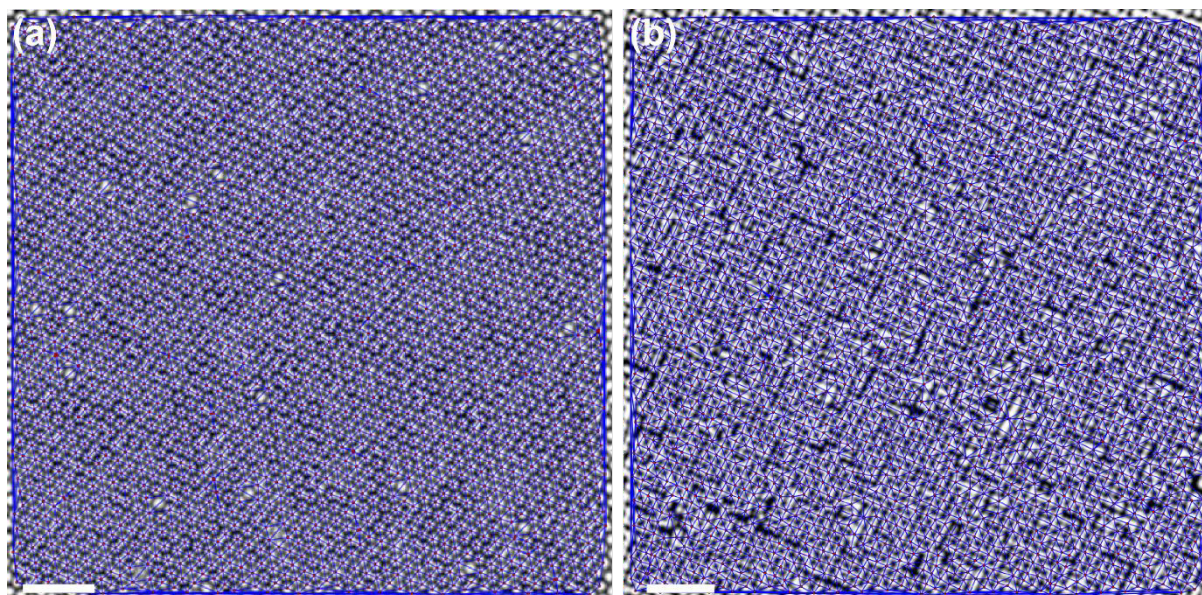
131 **Figure S12: Calculation of the X-ray penetration depth as a function of incident angle.** The red, purple
 132 and orange lines depict the penetration depths as function of incident angle for PbSe, ethylene glycol
 133 and toluene respectively. The blue dashed lines show the incident angle of the experiments (0.3°) and
 134 the corresponding penetration depth for PbSe (16.3 nm). Working at the critical angle of either
 135 toluene or ethylene glycol would result in a minute penetration of the X-ray photons into the PbSe
 136 superstructure.

137 **Supplementary methods 2: computer aided image analysis**

138 To determine the bond-angles, average NC-NC distances and surface density, we employed computer
139 aided image analysis. The code used was written in the Python scientific programming language, with
140 the addition of the numpy, matplotlib, scipy and opencv libraries.

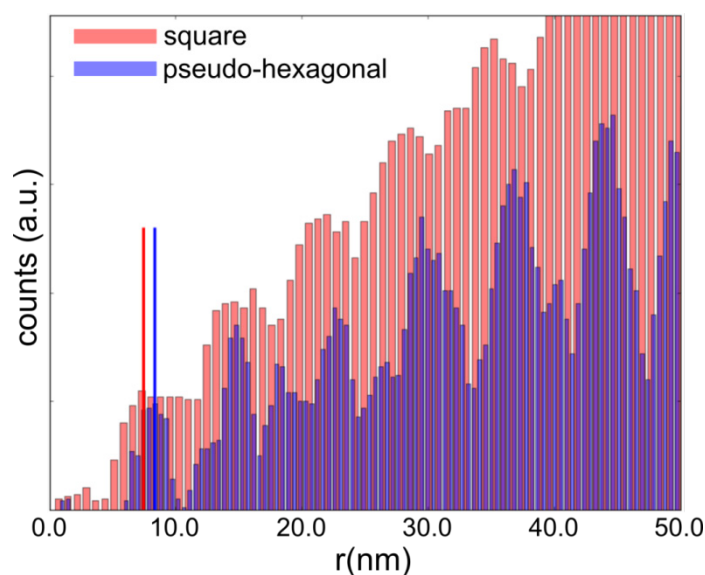


158 **Figure S13: Schematic overview of the computer aided image analysis as performed in Python. (a)** A
159 TEM image is loaded into the program. **(b)** The TEM image is low-pass filtered with a 2D Gaussian ($\sigma <$
160 0.6 nm) to remove 'salt-and-pepper' noise. **(c)** A spherical template of a dark particle on a white
161 background is created and the cross correlation (CC) of the template with each pixel on the filtered
162 image is calculated and averaged over multiple sizes of the spherical template. **(d)** The CC image is
163 binarized and the centers of mass (COM) of the segments are determined. **(e)** COMs within 15 pixels
164 of the image edge (red spots) are discarded to avoid edge artefacts. **(f)** On the remaining COMs a
165 Delaunay triangulation was performed (blue mesh over the image).



166 **Figure S14: Computer aided image analysis on the TEM images. (a)** The pseudo-hexagonal phase and
 167 **(b),** the square phase. The red dots indicate the centers of mass, the blue mesh is the Delaunay
 168 triangulation over these centers of mass.

169



170 **Figure S15: Radial distances obtained from the detected centers of mass for the PH phase (blue) and**
 171 **square phase (red).** The blue and red vertical lines indicate the average NN distances for the PH and
 172 square phases respectively.

173

174 First, the centers-of-mass (COMs) of the PbSe NCs are automatically recognized using the procedure
 175 outlined in Figure S13. Next, from the COMs and the Delaunay triangulation the inter-particle
 176 distances and bond angles are determined. Furthermore from the surface area of the convex hull of
 177 the triangulation and the number of COMs, the number of particles per unit surface was determined.

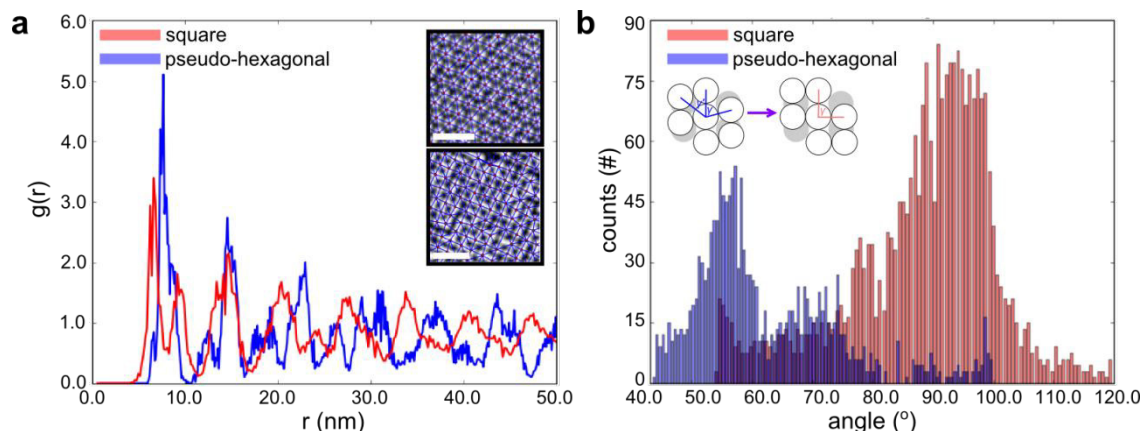
178 From the histogram of the radial distances, the pair distribution function was extracted:

$$g(r) = \frac{\# \text{ particles at distance } r}{2\pi r \cdot dr \cdot \rho \cdot N}$$

179 Where $g(r)$ is the pair distribution function, dr is the thickness of the circular shell at distance r , ρ is
 180 the average density of particles per unit surface and N the total number of detected particles.

181

182



183 **Figure S16: Image analysis on the PH and square phase TEM images.** (a) Pair distribution function
 184 obtained from the detected centers of mass of the PH phase (blue) and square phase (red). The large
 185 number of oscillations is a signature of extended positional order in the superlattice. The insets show
 186 the detected particles with the Delaunay triangulation mesh for the PH (top) and square (bottom)
 187 phase. (b) Bond angles of the superlattice in the PH (blue) and square phases (red). The inset shows a
 188 schematic of the two phases displayed on top of a perfect hexagonal crystal (grey dots). Scale bars in
 189 the TEM inset are 25 nm.

190 To further analyze the intermediate phases occurring in the oriented-attachment process, we
 191 performed computer aided image analysis on the real-space TEM images of Fig. 1(g) and 1(k). Fig. 3(a)
 192 shows the pair distribution function of the NC–NC distances extracted for the pseudo-hexagonal
 193 (blue) and the square (red) phase. The nearest-neighbor distances decreases from 8.3 ± 0.3 nm for the
 194 PH phase to 7.4 ± 0.3 nm for the square phase (see Fig. S15). The contraction calculated from TEM
 195 images (11%) is smaller than that obtained from GISAXS (17%), as we could not isolate the pure
 196 hexagonal phase ex-situ. The bond angles of the superlattice are determined from the Delaunay
 197 triangulation, as shown in Fig. S16(b). The appearance of the 55° and 70° angles in the PH phase (blue
 198 bars) combined with the 2:1 peak intensity ratio are indicative for the deviation from a perfect
 199 hexagonal lattice. The square phase (red bars) has bond angles close to 90° (see Fig. S8).

200

201 The code for the automated particle detection is available online at:

202 <http://www.filedropper.com/imageanalysisbrightfieldtem>

203 or by emailing to j.j.geuchies@uu.nl.

204 **Supplementary methods 3: modeling of GISAXS patterns for hexagonal, rhombic and square**
 205 **superlattices**

206 We model scattering by the NC superlattice following a method [1,2] within the quasi-kinematic
 207 approximation. The NCs are modeled as spheres of radius R , for which the form factor is

$$P(q, R) = \left(3 \frac{\sin(qR) - qR \cos(qR)}{(qR)^3} \right)^2$$

208 where $q = \sqrt{q_{\parallel}^2 + q_z^2}$ is the total scattering vector, q_{\parallel} is the in-plane component, and q_z the out-of-
 209 plane component.

210 The structure factor of the 2-D crystal as a function of bond angle is calculated from the direct-space
 211 unit cell vectors. The resulting reciprocal lattice vectors \mathbf{b}_1 and \mathbf{b}_2 are used to calculate the reciprocal
 212 lattice. The diffraction condition is met for any scattering vector \mathbf{q} that matches a reciprocal lattice
 213 vector \mathbf{G} . The total pattern (up to some value of q) is therefore obtained by summing over a range of
 214 h and k values:

$$S(q_{\parallel}) = \sum_{h=-3}^3 \sum_{k=-3}^3 L(q_{\parallel}, h\mathbf{b}_1 + k\mathbf{b}_2)$$

215 where

$$L(q_{\parallel}, \mathbf{G}) = \frac{(2\pi|q_{\parallel}|)^{-1}}{[1 + \Gamma^{-1}(q_{\parallel} - |\mathbf{G}|)]^2}$$

216 is the Lorentzian line shape of each individual diffraction, with peak width Γ and centered at $|\mathbf{G}|$.

217 The effect of reflections on the liquid–gas interface is described by a Vineyard factor as:

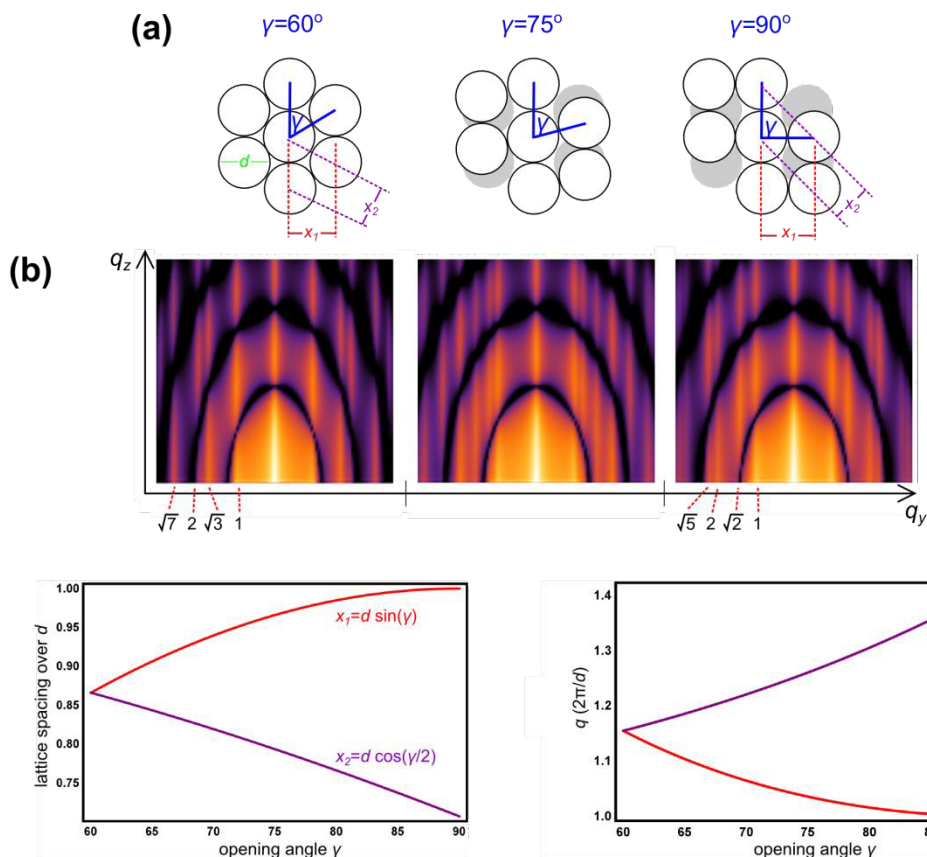
$$V(q_z) = \left\{ \begin{array}{ll} 0 & \text{for } q_z < k_0 \sin \alpha_i \\ \left| \frac{2 k_{fz}}{k_{fz} + \sqrt{k_{fz}^2 + (k_0 \sin \alpha_c)^2 + iv}} \right|^2 & \text{for } q_z \geq k_0 \sin \alpha_i \end{array} \right\}$$

218 Here $k_0 = 2\pi/\lambda$, $k_{fz} = q_z - k_0 \sin(\alpha_i)$, α_c is the critical angle of the interface, α_i the angle of
 219 incidence, and $v = \beta/\delta$, where β and δ describe the refractive index of the sample $n = 1 - \delta + i\beta$.
 220 Since v is in the order of magnitude of 10^{-2} - 10^{-3} for X-rays, we neglected this term in the simulations.

221 The total scattered intensity is then calculated as:

$$I(\mathbf{q}) = P(q, R) S(q_{\parallel}) V(q_z)$$

222 It should be noted that the complete scattering pattern could be predicted in greater detail, including
 223 multiple scattering events, using the distorted-wave Born approximation, which goes however
 224 beyond the scope of this work.



225 **Figure S17: Simulated GISAXS pattern as function of bond angles.** (a) The three models which were
 226 calculated: a 2-D hexagonal crystal, a 2-D crystal with a bond angle of 75° and a 2-D square crystal.
 227 The lattice planes that are equivalent in the hexagonal crystal (x_1 and x_2) break their degeneracy when
 228 the bond angle is changed from 60° to 90° . Here, d equals the diameter of the spheres. (b) Calculated
 229 GISAXS patterns for the corresponding 2-D crystals. Note how all diffraction rods split when the
 230 opening angle is 75° . Also note that for the 2-D square crystal the first higher order diffraction rod
 231 (indicated with $\sqrt{2}$) coincides precisely with the first form-factor minimum at low values of q_z . (c) The
 232 change of the relative lattice spacings x_1 and x_2 over d , when going from the 2-D hexagonal crystal to
 233 the 2-D square crystal in direct space (left) and reciprocal space (right). Note how the degeneracy is
 234 lifted when the bond angle differs from 60° .

235 **Supplementary methods 4: calculation of the position of the atomic reflections on the GIWAXS detector**

236 We want to obtain the peak position of the atomic diffraction when the nanocrystals are aligned not
 237 only in the 2θ -direction but also in the φ -direction. We put the center of the sample surface at the
 238 origin of our coordinate system, the z-axis to be along the X-ray beam, the x-axis perpendicular to the
 239 sample surface and the y-axis perpendicular to both. The x-component of the scattered wavevector
 240 written in polar coordinates is:

$$k_{\text{out},x} = |\mathbf{k}_{\text{in}}| \sin \theta_p \cos \varphi$$

241 The component θ_p is the polar angle the scattered beam makes with respect to the z-axis, which is
 242 equal to the Bragg angle (2θ), and can be calculated with the Bragg equation. The magnitude of the
 243 incoming X-ray wavevector, $|\mathbf{k}_{\text{in}}|$, is given by $2\pi/\lambda$. The x-component of the outgoing wavevector,
 244 $k_{\text{out},x}$, can be calculated by addition of a reciprocal lattice vector to $k_{\text{in},x}$

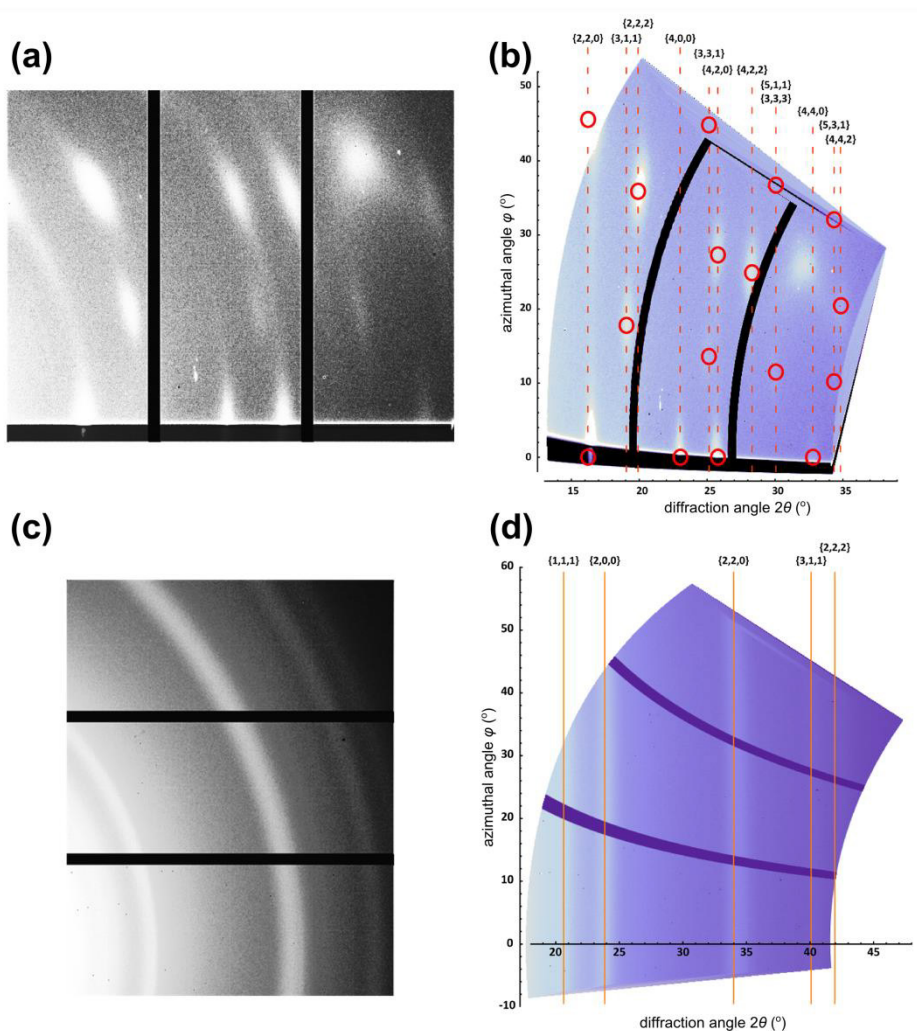
$$k_{\text{out},x} = k_{\text{in},x} + g_h$$

245 As the nanocrystals are oriented on the surface, they are only free to rotate around the x-axis. The x-
 246 component of the reciprocal lattice vector, g_h , is unaffected by rotations around the x-axis and
 247 therefore remains $2\pi h/a$. In which h is the Miller index the x-direction and a is the lattice spacing of
 248 rock salt PbSe. As this crystal structure possesses cubic symmetry (space group $Fm\bar{3}m$), the h , k and l
 249 components of the reciprocal lattice are interchangeable. The x-component of the incoming X-ray
 250 wavevector, $k_{\text{in},x}$, is equal to zero, as we have chosen our z-axis to be parallel to the X-ray beam. If we
 251 now plug in the resulting $k_{\text{out},x}$ back in our first equation, we have a complete description of the θ
 252 and φ values for every possible reflection $\{h,k,l\}$;

$$\theta = \sin^{-1} \left(\frac{\lambda \sqrt{h^2 + k^2 + l^2}}{2a} \right)$$

$$\varphi = \cos^{-1} \left(\frac{h \cdot \lambda}{2\pi \cdot \sin 2\theta} \right)$$

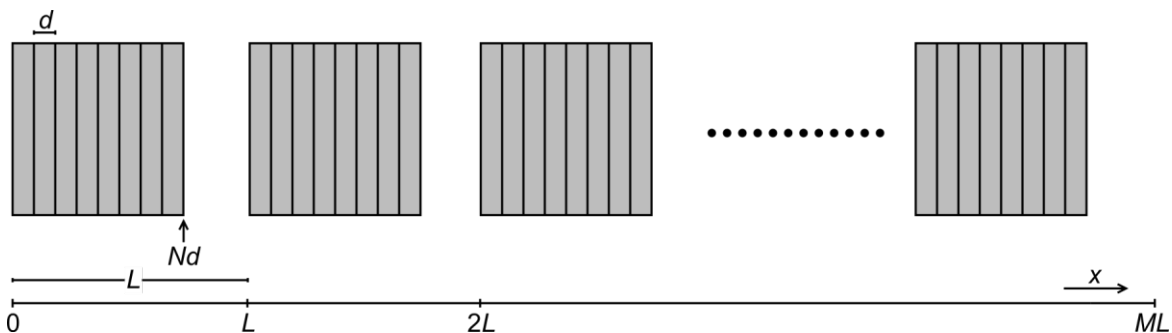
253



254 **Figure S18: GIWAXS parametrization and data analysis.** (a) Atomically aligned NCs on top of a Si-(100)
 255 substrate with their [100] axis perpendicular to the surface, giving rise to diffraction spots on the
 256 GIWAXS detector. (b) Same image, after coordinate transformation from pixel values to 2θ and ϕ
 257 values. The red dots are the positions of the expected atomic reflections. The only unlabeled
 258 diffraction peak at $(2\theta, \phi) = (32^\circ, 28^\circ)$ corresponds to a Si reflection, the sample substrate. These
 259 GIWAXS patterns were recorded during initial experiments at an X-ray energy of 20.7 keV. (c) GIWAXS
 260 of the PbSe NCs in solution. These are identical particles to those used for the in-situ experiments in
 261 the main text. (d) Transformed GIWAXS image, showing the position of the diffraction rings.
 262 Experiments recorded with the same experimental parameters as the in-situ experiments.

263 **Supplementary methods 5: peakwidth of atomically aligned, but not attached, nanocrystals**

264 The diffraction signal is as a first order approximation equal to the squared Fourier Transform of the
 265 electron density profile. We approximate the NC superlattice here as a one-dimensional chain of
 266 connected crystal and we consider the horizontal [100] direction. The lattice vector in the [100]
 267 direction equals 6Å. Each NC consists out of N (100) planes in the horizontal direction, for the NCs
 268 used in the experiments $N= 8-10$. The length from the start of a nanocrystal to the next nanocrystal
 269 is L and the total chain consists out of M of these repeating units in the positive x direction.



270 **Figure S19: nanocrystal model used to approximate the peak widths.** Each nanocrystal has a N
 271 lattice planes with a lattice spacing d . The length from the start of the NC to its neighbour equals L .

272

273 The Fourier Transform of this chain of *separated, but aligned*, nanocrystals is given by

$$F(q) = \int_0^{ML} \rho(x) e^{-iqx} dx$$

274 which can be split into a sum of repetitions of the first segment

$$F(q) = \sum_{j=0}^{M-1} \int_{0+jL}^{L+jL} \rho(x) e^{-iqx} dx$$

275 This summation can be expanded as

$$\begin{aligned} F(q) &= \int_0^L \rho(x) e^{-iqx} dx + \int_L^{2L} \rho(x) e^{-iqx} dx + \int_{2L}^{3L} \rho(x) e^{-iqx} dx + \dots + \int_{(M-1)L}^{ML} \rho(x) e^{-iqx} dx \\ &= \int_0^L \rho(x) e^{-iqx} dx + \int_0^L \rho(x) e^{-iq(x+L)} dx + \int_0^L \rho(x) e^{-iq(x+2L)} dx \dots \\ &= \sum_{j=0}^{M-1} e^{-iqLj} \int_0^L \rho(x) e^{-iqx} dx \end{aligned}$$

276 The summation above has a general solution, given by

$$S_N = \sum_{n=0}^N a_0 q^n = a_0 \frac{q^{N+1} - 1}{q - 1}$$

277 Hence the summation outside of the integral is given by

$$\sum_{j=0}^{M-1} e^{-iqLj} = \frac{e^{-iqML} - 1}{e^{-iqL} - 1}$$

278 The integral itself, which runs over a single segment of length L can be evaluated in an equivalent
 279 manner:

$$\int_0^L \rho(x)e^{-iqx} dx = \int_0^{Nd} \rho(x)e^{-iqx} dx + \int_{Nd}^L \rho(x)e^{-iqx} dx$$

280 The second integral is equal to zero as there is no electron density in between the nanocrystals. The
 281 second integral is evaluated equivalently to the summation over all nanocrystals and gives

$$\int_0^{Nd} \rho(x)e^{-iqx} dx = \frac{e^{-iqNd} - 1}{e^{-iqd} - 1} \int_0^d \rho(x)e^{-iqx} dx = \frac{e^{-iqNd} - 1}{e^{-iqd} - 1} S_n$$

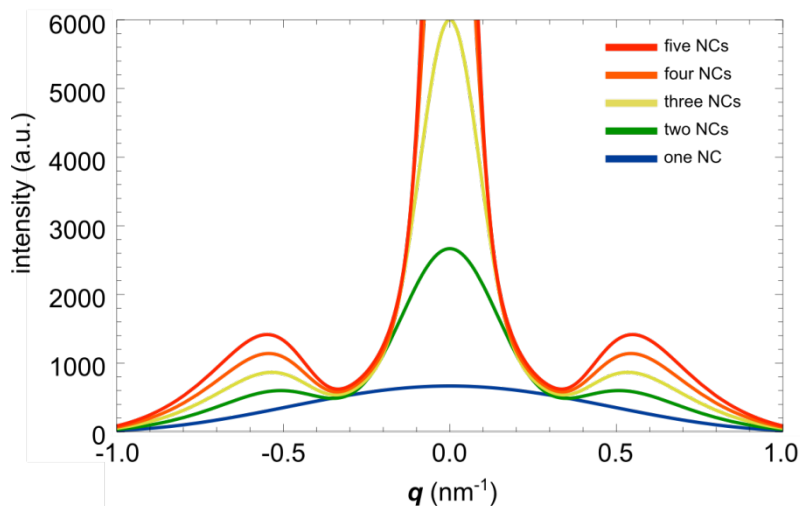
282 Where we treat the Fourier Transform of the electron density in between the lattice planes, S_n , as a
 283 constant.

284 The intensity is measured as $|F(q)|^2$ and can now be approximated by:

$$I(q) \propto \frac{\sin^2\left(\frac{qML}{2}\right) \sin^2\left(\frac{qNd}{2}\right)}{\sin^2\left(\frac{qL}{2}\right) \sin^2\left(\frac{qd}{2}\right)}$$

285 We assume a perfect positioning of the nanocrystals in the above derivation. This situation is not
 286 realistic, but can be improved by assuming a Gaussian distribution of the nanocrystal positions:

$$I(q) \propto \int_0^\infty e^{-\frac{1}{2}\left(\frac{L-L_0}{\sigma L}\right)^2} \frac{\sin^2\left(\frac{qML}{2}\right) \sin^2\left(\frac{qNd}{2}\right)}{\sin^2\left(\frac{qL}{2}\right) \sin^2\left(\frac{qd}{2}\right)} dL$$



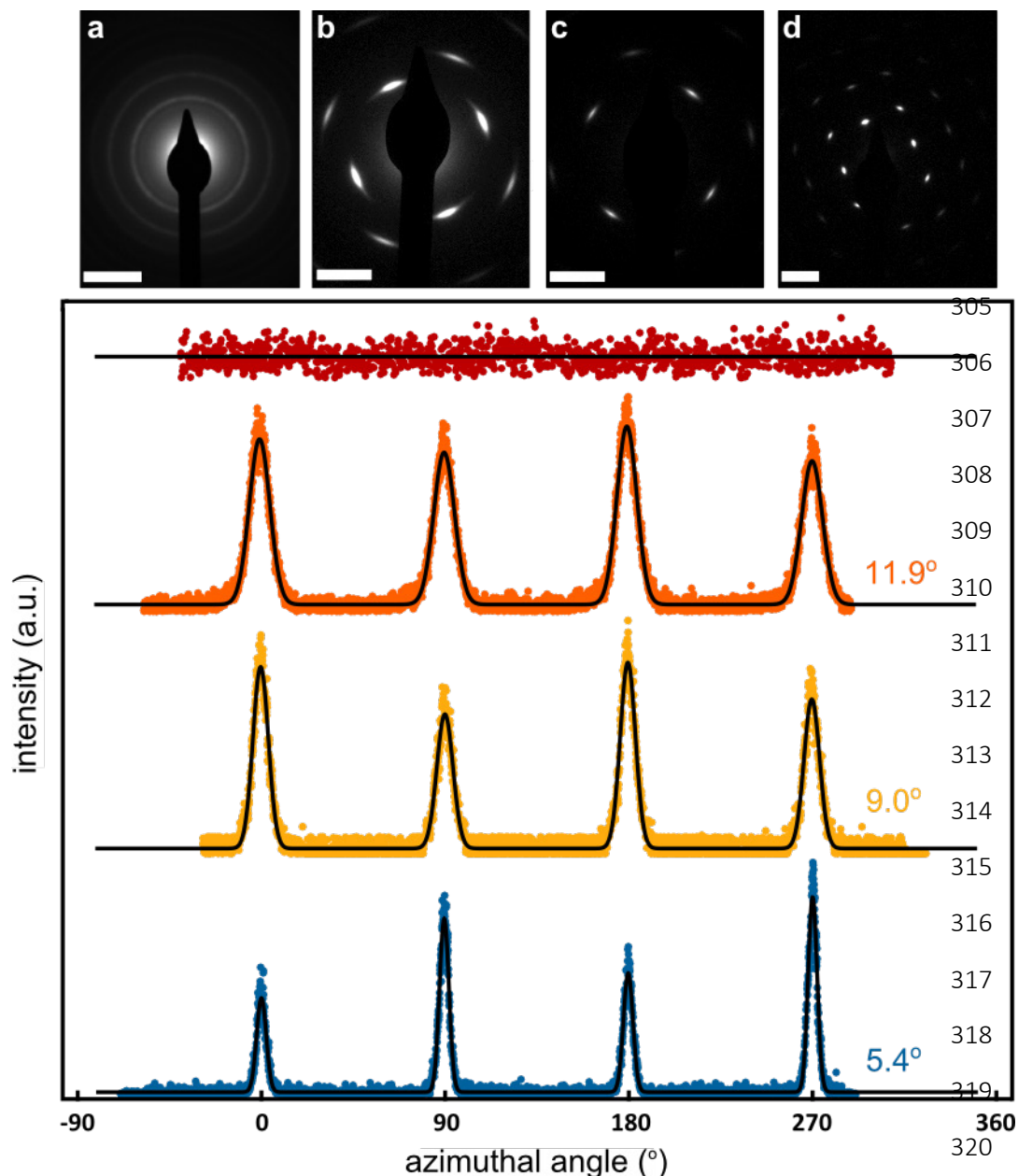
287 **Figure S20: peak width of aligned but not connected nanocrystal as a function of increasing**
 288 **number of attached nanocrystals.** Plotted are the scattering curves using $d = 0.6$ nm, $N = 9$ (the
 289 product $N*d$ gives a realistic nanocrystal size), $L_0=1.53*N*d$. We used $\sigma L = 0.4*L_0$.

290 It can be seen that the peak width decreases slightly upon increasing the number of aligned
 291 particles, due to the variations in the nanocrystal positions, assumed to mimic the in-situ
 292 experimental conditions.

293 The approximation used above is only accounting for a variation in the particle positions. When we
294 assume further disorder by considering the NC rotational freedom along all three Cartesian axes, the
295 peak width of the diffracted signals will decrease even less.

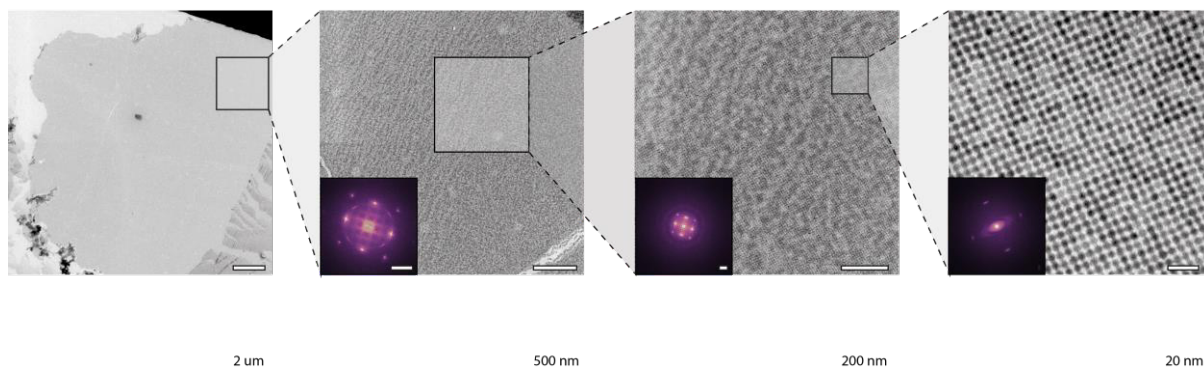
296 Upon perfect alignment of the particles (no rotational misalignment, no distribution in the particle
297 positions) the peak width decreases. However, we consider the latter situation to be unrealistic and
298 do assign the decrease in atomic peak width to be due to particle attachment.

299 **Supplementary methods 6: azimuthal and radial peakwidths in electron diffraction**

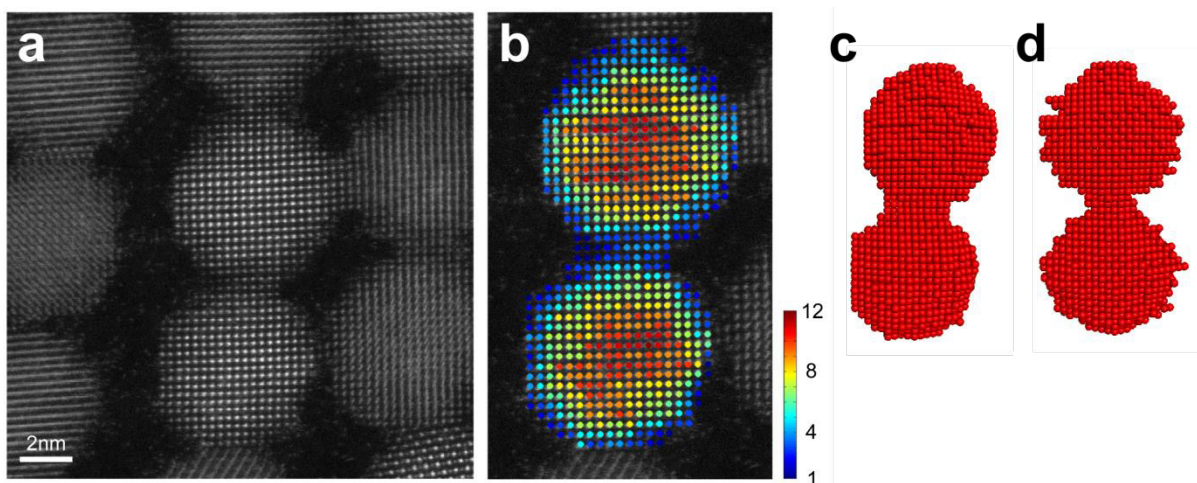


321 **Figure S21: azimuthal peak widths of the electron diffraction patterns during the self-assembly process.**
 322 ED patterns and azimuthal traces over the {400} reflection show a decrease in peak width,
 323 which indicates the loss of in-plane rotational freedom of the nanocrystals during the self-assembly
 324 process.

325 Azimuthal traces over the {400} reflections from the electron diffraction patterns in the main text are
 326 presented in the figure above. Going from completely disordered NCs (Fig. S20(a)) to the square
 327 superlattice with attached nanocrystals (Fig. S20(d)) the peak widths of the {400} reflections decrease,
 328 showing that the nanocrystals have less in-plane rotational freedom with respect to each other. We
 329 should remark here that the data should not be interpreted in a quantitative way, as instrumental
 330 broadening is not taken into account here.



331
 332 **Figure S22: Conservation of nanocrystalline order on mesoscopic length scales.** From left to right
 333 consecutive zoomed in TEM images are displayed, which show a very long-range periodicity. Even
 334 though the atomic coherency throughout the complete lattice is conserved over several nanocrystals,
 335 this does not perturb the long-range nano-crystalline order. From the widths of the $\{100\}$ -superlattice
 336 reflections in the Fourier transforms we obtain nanocrystal coherence lengths for the superlattice of
 337 39.3 nm, 34.3 nm and 35.9 nm from left to right. Scale bars from left to right images are 2 μm , 500 nm,
 338 200 nm and 20 nm respectively and 1 nm^{-1} for all Fourier transform insets.



339 **Figure S23: HAADF-STEM and atom counting reconstruction on attached NCs.** (a) HAADF-STEM image
 340 of NCs attached in a square superlattice. The atomic periodicity is continued from a given NC to its
 341 neighbors. Slight misorientations can also be observed. (b) Results from the atom counting procedure,
 342 using (a) as an input image. The color bar represents the number of detected atoms in each vertical
 343 column. (c) Top-view and (d) side-view of the reconstructed atomic model.

344 **Supplementary methods 7: Coulomb and Van Der Waals interactions between nanocrystals**

345 We model the interaction between two PbSe nanocrystal cubes (consisting out of 3375 atoms)
 346 through electrostatic and Van Der Waals interactions. We assume an ionic model for rocksalt PbSe.
 347 For the calculation of the Coulomb potential between two nanocrystals, we sum the Coulomb
 348 potentials of each ion in nanocrystal 1 in interaction with all ions in nanocrystal '2'. This is performed
 349 for a given relative position of nanocrystal 1 with respect to nanocrystal 2. Hence the Coulomb
 350 interaction is given by:

$$V_{coulomb} = \frac{1}{4\pi\epsilon_0} \sum_i^{N_i} \sum_j^{N_j} \frac{q_i q_j}{r_{ij}}$$

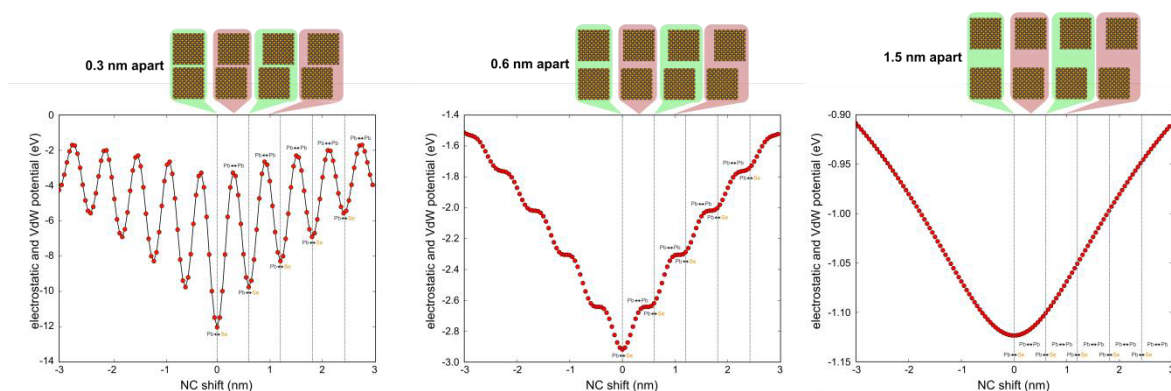
351 Where With ϵ_0 the vacuum permittivity, q_i and q_j the charges on atom 1 (located in nanocrystal 1) and
 352 atom 2 (located in nanocrystal 2). The double sum runs over all pairs of atoms in nanocrystal i and
 353 nanocrystal j .

354 The Van Der Waals interaction is calculated as spontaneous dipole-induced dipole (otherwise known
 355 as London or dispersion interactions);

$$V_{VdW} = -\frac{3}{2} \sum_i^{N_i} \sum_j^{N_j} \frac{I_i I_j}{I_i + I_j} \frac{\alpha_i \alpha_j}{r_{ij}^6}$$

356 With I_i and I_j the first ionization energies of atom 1 and 2 and α_i and α_j the polarizabilities of atom 1
 357 and 2. Again both atoms are located in nanocrystal 1 and nanocrystal 2 respectively. For Pb the first
 358 ionization energy equals 715,6 kJ/mol and the polarizability equals 6.8 \AA^3 . For Se the first ionization
 359 energy equals 715,6 kJ/mol and the polarizability equals 6.8 \AA^3 .

360



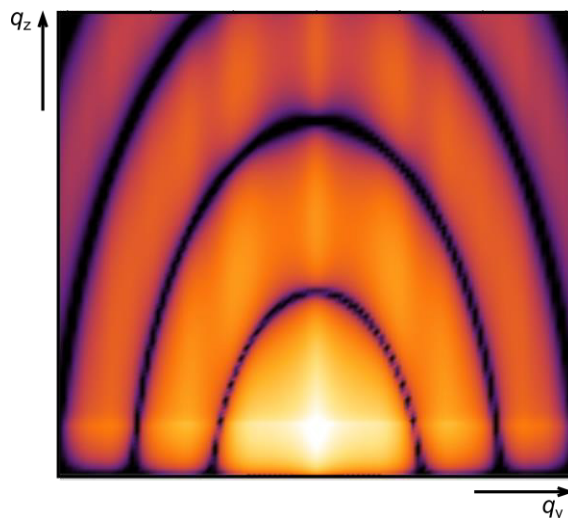
361 **Figure S24: The interaction between two nanocubes of PbSe upon lateral displacement.** The left, middle
 362 and right images shows the interaction potential when the nanocrystals are 0.3 nm, 0.6 nm and 1.5
 363 nm apart respectively.

364 When we start from the ideal situation, i.e. the nanocrystals are exactly opposing each other and Pb
 365 ions face Se ions, the energy is strongly increased upon moving the nanocrystals half a unit cell along
 366 the x-axis because of direct short range repulsions.

367 At a distance of 0.3 nm (left image in Fig. S23), the oscillations of the interaction potential have the
 368 same period as the unit cell and are quite pronounced. When we increase the distance between the
 369 nanocrystals to 0.6 nm, these oscillations are still visible, indicating preferential orientation of the

370 atomic lattices favoring Pb-to-Se alignment. The 0.6 nm distance approaches realistic experimental
371 conditions. When we further increase the distance to 1.5 nm, the oscillations disappear, but there is a
372 general potential minimum when the nanocrystal [100] facets have maximum overlap. Such a
373 potential leads an attractive driving force between the nanocrystals for maximum {100} to{100} facet
374 overlap, be it with half a unit cell mismatch to maximize the interactions between ions of opposite
375 charge.

376 In the simulations of the hexagonal to square phase transitions, the above potential is mimicked by
377 attractive patches centered on the vertical {100} facets of each nanocrystal, representing a similar
378 driving force for maximal facet-to-facet overlap as following from the atomistic calculations.



379 **Figure S25: Expected GISAXS pattern for a slightly oblique square lattice.** Calculated for a slightly
380 distorted square lattice with a bond angle of 83° and additional broadening due to the small
381 superlattice grain size. Note the agreement with the experimental GISAXS patterns obtained during
382 the in-situ experiments.

383 **References**

- 384 1. Heitsch, A. T., Patel, R. N., Goodfellow, B. W., Smilgies, D.-M. & Korgel, B. A. GISAXS
385 Characterization of Order in Hexagonal Monolayers of FePt Nanocrystals. *J. Phys. Chem. C*
386 **114**, 14427–14432 (2010).
- 387 2. Smilgies, D.-M., Heitsch, A. T. & Korgel, B. A. Stacking of hexagonal nanocrystal layers during
388 Langmuir-Blodgett deposition. *J. Phys. Chem. B* **116**, 6017–6026 (2012).